

# Numerical dissipation in RSPH simulations of protoplanetary disks

S. Børve<sup>1,2</sup>

steinabo@astro.uio.no

R. Speith<sup>3</sup>

speith@tat.physik.uni-tuebingen.de

J. Trulsen<sup>1</sup>

jtrulsen@astro.uio.no

*University of Oslo, Institute of Theoretical Astrophysics, P.O. Box 1029, Blindern, N-0315  
Oslo, Norway*

*Norwegian Defence Research Establishment, P.O. Box 25, N-2027 Kjeller, Norway*

*Institute for Astronomy & Astrophysics, University of Tübingen, Auf der Morgenstelle 10,  
D-72076 Tübingen, Germany*

## ABSTRACT

Smoothed Particle Hydrodynamics (SPH) is widely used for astrophysical applications, in particular problems of self-gravitational hydrodynamics. However, critics have argued that inherent accuracy problems with the method can be identified, in particular when it comes to describing shocks and dynamical instabilities. Regularized Smoothed Particle Hydrodynamics (RSPH) has previously been proposed as an extension to SPH. It is an attempt to increase the accuracy of the hydrodynamical description without having to abandon the Lagrangian formulation altogether. As the name implies, the method relies on a regularization technique where the solution at temporal intervals is mapped on to a new set of regularly placed particles. This technique allows us to reduce the numerical noise otherwise caused by highly irregular particle distributions and to take advantage of a more flexible approach to variable resolution. The cost of introducing the regularization scheme lies in increased methodical complexity, and in increased numerical dissipation. This paper investigates the numerical dissipation both qualitatively and quantitatively in the context of two-dimensional models relevant to the study of protoplanetary disks. Basic hydrodynamical tests

highlight key properties of the RSPH approach. By comparison with an analytical solution, we are also able to quantify the dependence of the spurious viscosity on key numerical parameters. To put the theoretical discussion in perspective, we also present results from simulations of test problems involving disk-planet interactions. The results are compared to published results obtained with other codes.

*Subject headings:* methods: numerical — hydrodynamics — accretion, accretion disks

## 1. Introduction

Grid-based, Eulerian methods have for a long time been used to study astrophysical fluids governed by the combined effects of gravitation, radiation, magnetic forces, and fluid flow. A wide range of codes exists, and a major research effort has been put into developing solvers that can handle the relevant combination of effects. However, the Eulerian formulation also has its limitations. First, complex, advective flows are challenging to model, in particular if multiphase descriptions are required. Secondly, three-dimensional structures, e.g. in self-gravitating systems, often have shapes not particularly well represented by rectangular grid cells. Thirdly, due to an otherwise overwhelming computational cost, it is often necessary to apply an adaptive approach when modelling astrophysical fluids in two and three dimensions. Implementing grid-based, adaptive schemes is still considered a fairly complex process.

Due to what has been perceived as fundamental limitations to Eulerian methods, alternative methods based on a Lagrangian formulation, both grid-based and gridless, have been developed. N-body methods focus on the gravitational interaction between a representative sample of individual particles (Aarseth 1963). Smoothed Particle Hydrodynamics (SPH) allows the treatment of gravitation to be combined with a description of the fluid dynamical effects (Lucy 1977; Gingold & Monaghan 1977). The method is Galilean invariant and can fairly easily incorporate a variable, density-dependent resolution. This opens up for a whole new range of applications which traditionally has not been within the scope of other methods. But the gridless approach also presents new challenges not found to the same extent with grid-based codes. For example, finding the best way to include magnetic forces and radiation in SPH simulations is still very much an area of research (Price & Bate 2007; Børve, Omang, & Trulsen 2006, hereafter referred to as Paper III; Whitehouse, Bate, & Monaghan 2005). Even when a purely hydrodynamical description is sufficient, critics claim SPH is considerably less accurate than comparable grid methods, in particular in regions

where the resolution ideally should be decoupled from the density (Kang et al. 1994; Klein 1999; de Val-Borro et al. 2006, hereafter referred to as VB06; Agertz et al. 2007).

Regularized Particle Hydrodynamics (RSPH) was developed with this in mind as an extension to SPH (Børve, Omang, & Trulsen 2001; Børve et al. 2005, hereafter referred to as Paper II). The aim has been to improve the overall accuracy and efficiency of SPH simulations without having to sacrifice the Lagrangian formalism altogether. This is achieved primarily through a regularization technique which allows the overall irregularities in the underlying particle distribution to be reduced and more general, problem-specific resolution criteria to be adopted. Secondly, the theoretical resolution, as determined by the smoothing length, is varied both in time and space by factors of two, much in the same way as in Adaptive Mesh Refinement (AMR) codes. RSPH has been shown to give good results on (magneto-)hydrodynamical shocks (Paper III; Omang, Børve, & Trulsen 2006). While the regularization scheme reduces the need for traditional artificial viscosity, the scheme introduces numerical effects such as increased dissipation and wave dispersion (Paper III; Børve, Omang, & Trulsen 2004, hereafter referred to as Paper I). These spurious effects are unavoidable as the regularization involves mapping the solution at a given point in time from an old to a new particle distribution.

In this paper, we investigate more closely the numerical dissipation caused by regularization in RSPH. This is done through a set of simulations relevant to the modelling of protoplanetary disks, although the dissipative effect is not restricted to this particular application. Protoplanetary disks were chosen as test application for several reasons. First, the study of protoplanetary disks is related to the understanding of planet formation and therefore of great interest. Secondly, the flow pattern in protoplanetary disks typically involves an inherent shearing motion which is expected to induce numerical dissipation during regularization. In fact, the ability of conventional SPH to handle shear flows has also recently been a matter of discussion (Imaeda & Inutsuka 2002; Monaghan 2006; Agertz et al. 2007; Price 2008). Thirdly, relevant models can be restricted to two dimensions making it feasible to study a wider range of important parameters.

This paper has been organized as follows: First, we will in §2 provide a short description of the method itself and the origin of the numerical dissipation. Then we present a selection of 3 basic hydrodynamical tests in §3. These tests illustrate the effect that regularization in general has on SPH simulations. Another test specifically relevant to the study of accretion disks, the viscous ring test, is discussed in detail in §4. This test is particular useful in that an analytic solution to the problem exists. It enables us to study the spurious viscosity both qualitatively as well as quantitatively. The dependence of the numerical dissipation on key numerical parameters is discussed. To put the discussion of numerical dissipation in

RSPH into perspective, we then present results from simulations of a planet-disk interaction in §5. This test was recently used in a comparative study of existing codes, including both grid-based and SPH codes (VB06). We will therefore compare our results to that provided in VB06, with a particular focus on possible effects of the numerical viscosity studied in detail in §4. Finally, a summary is given in §6.

## 2. The Numerical method

SPH is based on interpolation theory, and the equations of motion are expressed using integral interpolants, which in turn are approximated by summation interpolants. In the current work, the following set of equations are used to describe a hydrodynamic fluid (Monaghan 2005):

$$\frac{d\mathbf{r}_a}{dt} = \mathbf{v}_a, \quad (1)$$

$$\rho_a = \sum_b m_b \mathcal{W}_{ab}, \quad (2)$$

$$\frac{d\mathbf{v}_a}{dt} = - \sum_b m_b \left( \frac{P_b}{\rho_b^2} + \frac{P_a}{\rho_a^2} + \Pi_{ab} \right) \nabla_a \mathcal{W}_{ab}, \quad (3)$$

$$\frac{de_a}{dt} = \sum_b m_b \left( \frac{P_a}{\rho_a^2} + \frac{1}{2} \Pi_{ab} \right) \mathbf{v}_{ab} \cdot \nabla_a \mathcal{W}_{ab}, \quad (4)$$

$$P_a = (\gamma - 1) e_a \rho_a. \quad (5)$$

The mass, position, velocity, density, thermal pressure, and internal energy of particle  $a$  is denoted by  $m_a$ ,  $\mathbf{r}_a$ ,  $\mathbf{v}_a$ ,  $\rho_a$ ,  $P_a$ , and  $e_a$ , respectively. The interpolating kernel  $\mathcal{W}_{ab} = \mathcal{W}(\mathbf{r}_a - \mathbf{r}_b, h_{ab})$  has the characteristic scale length  $h_{ab} = (h_a + h_b)/2$  and should normalize to unity when integrated over all space. Where nothing else is specified, the commonly used third-order spline function is chosen as the interpolating kernel (Monaghan 2005). The quantity  $\Pi_{ab}$  is the commonly added artificial viscosity term as described by Monaghan & Gingold (1983). The strength of the artificial viscosity is determined by the two parameters  $\alpha$  and  $\beta$ . The treatment of spatially varying  $h$  in RSPH is somewhat different from that of conventional SPH and has been described in detail elsewhere (Paper II). To enable  $h$ -profile optimization (whenever  $h$  is allowed to vary) or to simply reduce particle disorder, a procedure called *particle regularization* is applied. This procedure, which represents the core difference between conventional SPH and RSPH, is the primary source for the additional numerical dissipation discussed in this paper.

Assume now that we want to replace an old particle distribution  $\mathcal{O}$  with a new particle distribution  $\mathcal{N}$ . The former distribution will in general be disordered due to the fluid flow

history, while the latter distribution typically is highly regular by design. When the spatial size and position of the old and the new particles are known, one can find the exact volume occupied by each particle using e.g. Voronoi diagram techniques (O’Rourke 1998). The right hand panel of Figure 1 illustrates this situation representing individual particles belonging to the old and new distributions by dots and plus signs, respectively. The corresponding Voronoi cells are indicated by solid and dotted lines, respectively. Based on the degree of spatial overlap between old and new particles, mass, momentum, internal energy etc. are transferred from  $\mathcal{O}$  to  $\mathcal{N}$ . Let summation indices  $o$  and  $n$  indicate particles belonging to  $\mathcal{O}$  and  $\mathcal{N}$ , respectively. If  $\Omega_n^o$  denotes the size of the spatial overlap between particles  $n$  and  $o$ , the mass of the new particle  $n$  is given by

$$m_n = \sum_o \frac{m_o}{\mathcal{V}_o} \Omega_n^o \quad (6)$$

where the equality

$$\mathcal{V}_o = \sum_n \Omega_n^o \quad (7)$$

determines the spatial size  $\mathcal{V}_o$  of the old particle  $o$  and thus secures conservation of mass. Generalised to linear momentum and internal energy per unit mass, we get

$$\mathbf{v}_n = \frac{1}{m_n} \sum_o \frac{m_o \mathbf{v}_o}{\mathcal{V}_o} \Omega_n^o, \quad (8)$$

and

$$e_n = \frac{1}{m_n} \sum_o \frac{m_o e_o}{\mathcal{V}_o} \Omega_n^o. \quad (9)$$

The left hand panel of Figure 1 illustrates a situation where a given old particle marked  $o$  finds overlap with 4 new particles marked  $n_1 - n_4$ . In this particular case, particles  $n_1$  and  $n_4$  inherit most of the mass, momentum, and internal energy of particle  $o$ , in roughly equal shares. Particles  $n_2$  and  $n_3$  on the other hand, inherit only small fractions of the same quantities. All 4 new particles, however, also inherit from other, overlapping particles of the old distribution. So in the end, the 4 new particles might very well end up with roughly the same mass, momentum, and internal energy.

## 2.1. The origin of numerical dissipation

While linear momentum and internal energy is conserved in this process, angular momentum and kinetic energy will not in general be exactly conserved. In particular, the kinetic energy will be reduced during regularization. To conserve total energy, a corresponding correction to the internal energy is applied. The regularization will therefore act as a

source of additional viscosity. No numerical viscosity is present where the velocity field is uniform. However, regularization can still have a dissipative effect, as a source of numerical diffusion. To illustrate this, we look at a force-free, one-dimensional system where a square pulse density profile exists. The particles representing this system is regularly placed with a particle spacing of  $\Delta$ . The initial width of the pulse is  $4\Delta$  and  $h = 1.4\Delta$ . All particles are assumed to move with the same drift velocity  $v_d$  with respect to the reference frame. At the temporal interval  $T_{\text{reg}}$ , hereafter referred to as the regularization period, a new particle distribution is generated as specified in equations (6)-(9). Due to the drift, the old and new particle distributions will in general be shifted relative to each other. This causes the density profile to broaden. This is shown in Figure 2 for 4 different cases. The ratio  $T_{\text{reg}}v_d/\Delta$  in simulations *a*, *b*, *c*, and *d* is equal to 0.01, 0.1, 0.5, and 1.0, respectively. There are 5 different curves in each of the 4 plots. The solid line indicates the initial density profile. The dotted, dashed, dash-dotted, and dash-triple-dotted lines show the solution in a co-moving reference frame after 100, 200, 300, and 400 regularizations, respectively. Unlike more realistic cases, the old and new particle distributions in this case always have the same shift relative to each other. As a result, we see in Figure 2 that the amount of diffusion depends highly on the drift velocity. Case *c* represents the maximum diffusion because the two distributions will be offset by exactly one half of a particle spacing. In case *d*, the drift velocity is such that the offset is exactly 0 and the numerical diffusion therefore vanishes as well. By comparing cases *a*, *b*, and *c* we can conclude that only a small offset relative to the particle spacing is required to get substantial numerical diffusion.

### 3. Basic hydrodynamic tests

In this section we study how regularization modifies the description of 3 basic, hydrodynamic problems. We also compare with results from grid codes. These tests illustrate both the effect of numerical dissipation due to regularization and the difference in how SPH and RSPH adopt variable resolution. The 3 tests include a linear wave test, a strong shock test, and a Kelvin-Helmholtz instability (KHI) test.

#### 3.1. Linear waves

Linear waves as a test case for SPH have primarily been of interest in relation to discussions on linear stability. In Morris (1996a,b) it was shown how linear stability in multi-dimensional simulations of hydrodynamical waves is only achieved when the ratio  $h/\Delta$  is close to 1.2. This result was later generalised to MHD waves (Paper I). The latter work

also discusses briefly how regularization might affect the dynamics of the waves. Generally speaking, the waves are strongly damped if the ratio of regularization period to wave period, hereafter referred to as  $r$ , is much less than unity. In the current work, we present test results of linear, isothermal waves. The simulation domain is  $2 \times 0.5$  in wave length units. Equal-mass particles initially placed on a uniform, Cartesian lattice are given small displacements resulting in a 0.1% amplitude density fluctuation. The  $h/\Delta$  ratio is set to 1.2 to insure linear stability. Since the commonly used third order B-spline kernel results in a fairly inaccurate phase speed for the current choice of  $h/\Delta$  (Morris 1996b), we instead use the fifth order B-spline kernel in this test. Simulations are performed for 5 different wave lengths ranging from  $12\Delta$  to  $192\Delta$ .

We are primarily interested in studying how the wave amplitude changes in time, and in particular we want to see to what extent regularization results in numerical dissipation which in turn causes the wave to be damped. The approach chosen in the current work, is to study the temporal evolution at a given sensor point. To be able to present the simulation results in a concise manner, we introduce the normalized damping rate,  $\gamma$ . Let us therefore assume that the density perturbation at the position of the sensor has the following form

$$\delta\rho(t) = \rho_1 e^{-\gamma\omega t} \cos(\omega t - \phi) \quad (10)$$

and let  $S_k$  denote the maximum absolute value of  $\delta\rho(t)$  measured by the sensor in the time interval  $t \in [kP_w, (k+1)P_w)$ , where  $P_w$  is the wave period. We look for the maximum perturbation over a full wave period because we are interested in the long term evolution of the amplitude. We can then calculate  $\gamma$  as a weighted average by the expression

$$\gamma = -\frac{2}{\Delta t\omega(N-1)N} \sum_{k=1}^{N-1} \ln\left(\frac{S_k}{S_0}\right), \quad (11)$$

where  $N = 100$  is the total number of simulated wave periods. Note that a positive  $\gamma$  indicates a decrease in amplitude. Figure 3 shows  $\gamma$  as a function of wave length for a number of different simulations. The solid lines indicate RSPH simulations where  $r$  vary from 0.75 to 16.25. We have deliberately avoided choosing integer values of  $r$  because this would result in smaller damping rates than one could normally achieve in more complex simulations. This is in line with what we observed in the force-free test discussed in §2.1. The dotted lines represent SPH simulations where the effect of adding artificial viscosity is studied. The viscosity parameter  $\alpha$  ranges from 0.0 to 1.0, while the relation  $\beta = 2\alpha$  holds for all simulations. The dashed line indicates results made with the grid code RH2D (Kley 1989).

From the solid lines we can conclude that regularization will dampen waves significantly if the regularization period is smaller than or similar to the wave period. As long as  $r$  is kept

more or less constant,  $\gamma$  is observed to vary only weakly with wave length. Likewise, the damping is negligible if the regularization period is an order of magnitude higher than the wave period. The SPH simulation with  $\alpha = 0$  is observed to show a slight increase rather than a decrease in the wave amplitude. This is due to inaccuracies in the time stepping scheme and can be reduced by reducing the time step. The amplitude growth can be seen to increase as the wave length is reduced from  $192\Delta$  to  $24\Delta$ . In the case of  $12\Delta$ , we therefore chose to reduce the time step. As a consequence, the  $\gamma$  becomes slightly positive in this case. When artificial viscosity is turned on, the SPH simulations even at the modest level of  $\alpha = 0.1$  show damping rates that are comparable or higher than that found in the RSPH simulations. The RH2D results show no signs of numerical dissipation. On the contrary, the same type of time stepping error seen in the inviscid SPH simulations, seems to be even more evident in the RH2D results as the latter results show clear indications of amplitude growth. Apart from this, none of the simulations described in this test show phase errors larger than 1% and regularization does not seem to affect this error significantly.

### 3.2. Strong shock with extreme jumps in pressure and velocity

The development of RSPH has in particular been motivated by the desire to improve the SPH treatment of shocks. Recent work also indicates, through comparisons with both numerical and experimental data, that this aim has been achieved (Paper II; Paper III; Børve et al. 2008; Omang et al. 2009). For the sake of completeness, however, we present a new comparison between RSPH and two other numerical methods on a shock tube problem. The current test was described by Xiao (2004) as a severe test problem not only in terms of numerical stability and robustness, but also when it comes to the conservative properties of the numerical method. In fact, non-conservative schemes tend to produce incorrect shock positions, especially in the case of strong shocks. The initial condition is defined within the computational domain  $0 \leq x \leq 1$  and consists of a left and right hand state separated by a membrane at  $x = 0.5$ . The initial state vector  $\mathbf{q} = (\rho, v, P)$  can be written in dimensionless units as

$$\mathbf{q} = \begin{cases} (1.0, 0.0, 1.0 \times 10^{10}) & \text{for } 0 \leq x \leq 0.5; \\ (0.125, 0.0, 0.1) & \text{otherwise.} \end{cases} \quad (12)$$

This initial condition creates a supersonic shock.

Figure 4 compares 3 different solutions of the density (left hand panel) and the velocity (right hand panel) at time  $t = 2.5 \cdot 10^{-6}$ . The solid line represents the RSPH solution obtained with a non-uniform, time-dependent resolution. Regularization is performed at variable intervals, typically around 70, according to a new, adaptive scheme (see Appendix A for more details). The standard ratio of smoothing length to particle spacing is here set

to 2.0. The dotted line represents the SPH solution obtained with equal-mass particles and with variable  $h$  (Price & Monaghan 2007). The last solution, represented by the dashed line, is made with the FCT solver included in the commercial software ANSYS AUTODYN<sup>1</sup> using a uniform grid. The latter code solves the problem on a one-dimensional grid with 1000 grid points. Both the SPH and RSPH solutions are the results of two-dimensional simulations. The time averaged particle number in the RSPH simulation is  $570 \times 11$ , while the particle number in the SPH simulation is fixed to 26000 ( $800 \times 32$  and  $100 \times 4$  in the high and low density regions, respectively). The SPH and RSPH results in Figure 4 have not gone through any post-processing but include the full particle data plotted along the  $x$ -axis.

The RSPH code is seen to handle the current problem quite well despite the severe initial condition. The shock interfaces are sharp and the shock positions and intermediate density and velocity levels fit well with both the results presented in Xiao (2004) and the AUTODYN results in Figure 4. There is however a noticeable overshoot near the shock front at roughly  $x = 0.85$ . The SPH code, on the other hand, has difficulties in handling the strong compression caused by the initial step in pressure. This leads to particle penetration, a well-known problem proposedly solved by modifying the equations of motion (Monaghan 1989). For the sake of comparison, however, we instead opted for the other common cure to this problem, namely to increase the artificial viscosity. Instead of the typical values of  $\alpha = 1$  and  $\beta = 2$ , we had to choose  $\alpha = 2$  and  $\beta = 4$  to prevent the particle penetration from occurring. The results still show clear indications of errors due to strong variation in particle spacing, such as the strong dip in density near the contact discontinuity. This indicates that the artificial viscosity is inefficient at preventing particle penetration in multi-dimensional simulations. Also, the shock interface is not very clearly defined. This is partly because the resolution drops by a factor of roughly 6 as density does the same, and partly because of the high level of artificial viscosity needed in this test.

### 3.3. Kelvin-Helmholtz instability

In Agertz et al. (2007) SPH is reported to perform poorly in tests relating to multiphase interactions. In particular, the authors are concerned about the SPH results of the Kelvin-Helmholtz instability (KHI) test. KHI, which occur when velocity shear is found at the interface between two fluids, is an important physical process for instance when considering gas cloud stability (Murray et al. 1993; Mori & Burkert 2000). In Agertz et al. (2007), the SPH results show no signs of instability growth for the density ratio  $\chi = 10$ . However, when

---

<sup>1</sup>Description available online at <http://www.ansys.com/products/explicit-dynamics/autodyn/>.

there is no density difference, that is  $\chi = 1$ , the KHI does indeed evolve more or less as in the grid results. They explain this fundamental difference by an artificial gap opening between the low and high density particles. In Price (2008), the error is attributed to a lack of dissipation associated with the jump in temperature found at the material interface. The author introduces an artificial conductivity term in the equations of motion which is shown to largely correct the SPH solution of the KHI. The instability is then observed both in the case of  $\chi = 2$  and  $\chi = 10$ .

Here we will present simulation results of the  $\chi = 10$  KHI test using RSPH. We will show results both with and without artificial conductivity. The simulation domain is, as in Agertz et al. (2007), chosen to be  $(-0.5 < x < 0.5) \times (0 < y < 0.5)$  with periodic conditions in  $x$  and reflecting conditions in  $y$ . In other words, we assume a symmetry line at  $y = 0$ . The density is 10 for  $y > 0.25$  and 1 for  $y \leq 0.25$  resulting in a density ratio of  $\chi = 10$ . The pressure is equal to 2.5 throughout. The ratio of specific heats,  $\gamma$ , is set to 5/3. The velocity components in  $x$  and  $y$  are given by

$$v_x = \begin{cases} 0.5 & \text{for } y < 0.25; \\ -0.5 & \text{otherwise} \end{cases} \quad (13)$$

and

$$v_y = \begin{cases} A \sin(-k(x + 0.5)) & \text{for } |y - 0.25| < 0.025; \\ 0 & \text{otherwise,} \end{cases} \quad (14)$$

where  $A = 0.025$  and  $k = 12\pi$ . No artificial viscosity is applied. A uniform resolution is used throughout with a standard particle spacing of  $1/256$  and  $h/\Delta = 1.2$ , and regularization is performed at fixed intervals of 48 time steps.

In Figure 5 we show two plots, marked **a** and **b**. Both plots show the solution at time  $t = \tau_{KH} = 0.58$ . These plots are directly comparable to the third row of plots (from the left) in Figure 13 of Agertz et al. (2007) and the third plot (from the left) in Figure 9 of Price (2008). The top plot shows results without artificial conductivity. Unlike the SPH results reported in Agertz et al. (2007), the perturbations have clearly grown, although the growth rate is not as large as that found in the grid solutions presented in Agertz et al. (2007). It is more similar to that presented in Price (2008), however the tip of each wave structure is not as thin. It is interesting to see how regularization in this case has a positive effect on the description of material interfaces. This is probably due to the numerical dissipation associated with it. As  $h/\Delta$  is increased, the ability to smooth the interface is gradually lost causing the results to look more like the inviscid SPH results. The effect that regularization has on the description of multiphase flow problems has recently been discussed in greater detail elsewhere (Børve & Price 2009). The bottom plot shows the effect of adding artificial conductivity as described in Price (2008). Due to the extra

dissipation, the transition between the high and low density region is smoother resulting in thinner wave tips. The growth rate is still not as large as that seen in the grid results in Agertz et al. (2007). The growth rate does, however, seem to be somewhat higher than that achieved with the standard SPH approach (Price 2008). Note also that the SPH results are obtained with equal-mass particles which, given the factor 10 density ratio, means a factor of 5.5 more particles are needed in the SPH simulations compared to the RSPH simulations.

#### 4. The viscous ring

A viscously spreading, pressure-less ring orbiting a central point mass  $M_c$  on Keplerian orbits is an important test case in the theory of accretion disks. It represents an idealized example of the main features of an evolving thin accretion disk, i.e. the inward transport of mass and outward transport of angular momentum (Pringle 1981). Under the assumption of a small kinematic viscosity  $\nu$  which is independent of the surface density, an approximate analytic solution can be found for this problem, stated originally by Lüst (1952) and later by Lynden-Bell & Pringle (1974) (for a more general solution see e.g. Speith & Riffert 1999).

The accretion disk is assumed to be thin, i.e. the vertical thickness of the disk is very small in comparison to the radial extent. The disk evolution can therefore be modelled by the vertically averaged hydrodynamic equations. This reduces the problem to two dimensions and formally corresponds to the two-dimensional version of the hydrodynamic equations. In particular, the density  $\rho$  is replaced by the vertically integrated surface density  $\Sigma$ . In this particular case, we will assume the initial surface density to be given as

$$\Sigma_{\text{init}}(R) = \frac{M}{2\pi R_0} \delta(R - R_0), \quad (15)$$

where  $M$  is the total ring mass. For a constant vertically averaged kinematic viscosity  $\nu_s$ , this leads to the following surface density solution of the viscously spreading ring (e.g. Lynden-Bell & Pringle 1974; Speith & Riffert 1999):

$$\Sigma(\tau^*, x) = \frac{M}{\pi R_0^2} \frac{1}{\tau^* x^{1/4}} I_{\frac{1}{4}}\left(\frac{2x}{\tau^*}\right) \exp\left(-\frac{1+x^2}{\tau^*}\right), \quad (16)$$

where  $x = R/R_0$  and  $\tau^* = 12\nu_s t/R_0^2$  are dimensionless radial and time coordinates, respectively. Furthermore,  $I_{\frac{1}{4}}$  denotes the modified Bessel function of order 1/4. It is important to realize that solution (16) fulfills the hydrodynamic equations only by approximation, assuming the kinematic viscosity  $\nu_s$  is small compared to the specific angular momentum  $R^2\sqrt{GM_c/R}$  in the disk. This is equivalent to the condition  $v_R \ll v_\varphi$ , where the azimuthal

velocity is equal to the Keplerian velocity

$$v_\varphi = \sqrt{\frac{GM_c}{R}} \quad (17)$$

and the radial velocity is obtained by

$$v_R = -\frac{3}{\Sigma\sqrt{R}} \frac{\partial}{\partial R} \left[ \nu_s \Sigma \sqrt{R} \right] \quad . \quad (18)$$

Figure 6 visualizes the surface density as a function of radius for several viscous times. This axi-symmetric, analytic solution of the viscous dust ring is frequently used as a test problem for numerical methods developed to simulate accretion disks (e.g. Flebbe et al. 1994; Speith & Riffert 1999; Kley 1999; Speith & Kley 2003). In fact, it is one of very few known analytic solutions for viscous flows. Therefore, it is also the basic test problem in this work.

#### 4.1. Simulations and results

To be able to simulate the evolution of the viscous ring, we include a module to handle shear viscosity in the RSPH code. Because we are only interested in deviations due to numerical diffusion, it is sufficient to adopt the common artificial viscosity approach of Monaghan & Gingold (1983) for modelling the kinematic shear viscosity. Using the relation developed by Meglicki, Wickramasinghe, & Bicknell (1993) we adjust the parameter  $\alpha$  of the artificial viscosity such that the underlying kinematic viscosity of the viscously dissolving ring is fixed to  $\nu_s = 4.8 \cdot 10^{-5}$  (in system units). It has to be noted though that for physically more realistic simulations of the viscous ring, a tensorial approach of the full viscous stress tensor should be adopted (Speith & Kley 2003).

The RSPH scheme is governed by three main numerical parameters. These are the regularization cycle  $c_r$ , the ratio of smoothing length to particle spacing  $h/\Delta$ , and the maximum smoothing length  $h$ . The regularization cycle  $c_r$  is the number of time steps between consecutive regularizations. The relation between  $c_r$  and regularization period  $T_{\text{reg}}$  is  $T_{\text{reg}} = \sum_{i=1}^{c_r} \Delta t_i$ , where  $\Delta t_i$  is the length of time step  $i$ . In this parameter study, we vary the regularization cycle according to  $c_r = 1, 2, 4, 8, 16, 32$  (measured in units of 40). The ratio of smoothing length to particle spacing is varied according to  $h/\Delta = 1.0, 1.2, 1.4, 1.6, 1.8, 2.0$ , while the smoothing length is fixed to  $h = 0.02 R_0$ . For the combination of  $c_r = 4$  and  $h/\Delta = 1.6$ , we additionally change the smoothing length  $h$  according to  $1000h = 15, 20, 25, 30, 35, 40$  (measured in the intrinsic length scale  $R_0$ ).

Initially, the RSPH particles are distributed on a 2D-annulus in the disk plane such that they represent the surface density of the ring at time  $\tau^* = 0.018$ . This avoids the

initial singularity of the viscous ring solution at  $\tau^* = 0$ . Snapshots of the RSPH solutions at  $\tau^* = 0.054, 0.090, 0.126, 0.162,$  and  $0.198$  are stored, and to evaluate the results, we compute the azimuthally averaged surface density as a function of the radial coordinate. The difference between the maximum and minimum density found at a given radius defines the noise level at that particular radius. By averaging over all radii, we obtain the noise error of the snapshot in question. Then, we determine an effective viscous time from a  $\chi^2$ -fit of the azimuthally averaged results against the analytic ring solution. This in turn allows us to calculate an effective kinematic viscosity  $\nu_{\text{eff}}$  for each simulation. This effective viscosity is the intrinsic physical kinematic viscosity  $\nu_s$  (modelled by artificial viscosity) modified by spurious numerical shear and numerical diffusion due to the regularization mechanism.

Figures 7, 8, and 9 show some of the RSPH results and how they depend on  $c_r$ ,  $h/\Delta$ , and  $h$ , respectively. In all diagrams, surface density is plotted against radial coordinate at simulation time  $\tau^* = 0.090$ . Solid lines denote the azimuthally averaged simulation results, the dotted lines indicate the upper and lower noise limits, the dashed line shows the analytic ring solution at  $\tau^* = 0.090$ , while the dashed-dotted lines depict the best fit of the analytic solution to the numerical results. Please note that panels 7 c), 8 d), and 9 b) represent the same simulation. A short regularization cycle (i.e. a large number of regularizations), causes the introduced effective dissipation to be rather high, as can be seen in Figure 7 a). Here, the ring has spread considerably wider than the corresponding analytic solution. In contrast, the noise error of the results is practically negligible in this case. With increasing  $c_r$ , the azimuthally averaged simulation results match the analytic solution better and better, while the noise at the same time grows significantly. The effective viscosity depends to a lesser degree on the number of particle spacings per smoothing length and on the value of the smoothing length, as can be seen by comparing Figures 8 and 9 to Figure 7. In the simulations corresponding to Figures 8 and 9  $c_r = 4$  is chosen. The azimuthally averaged surface density is seen to only marginally underestimate the analytic solution with slightly growing difference for decreasing  $\Delta/h$  and increasing  $h$ . The level of noise, however, is strongly increasing with decreasing  $\Delta/h$  and increasing  $h$ , in particular towards the inner ring boundary, where the velocity is higher.

A more quantitative evaluation of the effective viscosity based on all simulations can be found in Figure 10. For every simulation, i.e. for every combination of parameters  $c_r$ ,  $h/\Delta$  and  $h$ , a time-averaged  $\nu_{\text{eff}}$  is obtained. The error bars indicate the maximum and minimum value of the effective viscosity found during the time evolution of the viscous ring. The upper panel of Figure 10 shows the mean effective viscosity plotted as a function of regularization cycle  $c_r$ , where different curves indicate different values of  $h/\Delta$ . Accordingly, the middle panel shows  $\nu_{\text{eff}}$  plotted as a function of  $h/\Delta$  for the different values of  $c_r$ . The simulations in both diagrams use  $h = 0.02 R_0$ . In the lower panel,  $\nu_{\text{eff}}$  is plotted against

smoothing length  $h$ . Here,  $c_r = 4$  and  $h/\Delta = 1.6$  are adopted. In all three diagrams, the value for the intrinsic kinematic viscosity  $\nu_s$  is also indicated.

The relation between  $\nu_{\text{eff}}$  and the numerical parameters is as expected. Increasing the total number of regularizations performed (i.e. decreasing  $c_r$ ), causes the induced numerical diffusion to be increased as well. On the other hand, increasing the ratio  $h/\Delta$  of particle spacings per smoothing length, causes the spurious numerical viscosity to be reduced. Note, however, that the combination of small initial values of  $h/\Delta$  and large values of  $c_r$  is more likely to lead to insufficient interactions per particles. This is because the distance between particles increases during the spreading of the ring. If this is indeed the case, additional spurious effects can become important. Bear in mind that due to the variable length of the time steps, the regularization period  $T_{\text{reg}}$  may not be a constant in these simulations. This can possibly also influence the value of the effective kinematic viscosity, as the number of regularizations per time (and thus the introduced diffusion) increases when the time steps get shorter. Regarding the smoothing length, the effective viscosity is only increasing very slightly with increasing  $h$  (see lower panel of Figure 10). Apparently, the number of interaction partners is somewhat more important for the induced numerical diffusion than the total particle number, and both are much less important than the period of regularization.

An evaluation of the noise level in the simulations has also been performed and the results are summarized in Figure 11. The upper panel, where the noise error is plotted as a function of the number of regularization cycles, demonstrates nicely the advantage of the RSPH approach. For a high number of regularizations, the noise in the simulations is decreasing nearly linearly. We measured a noise error dependence of  $\sim c_r^{0.75}$  to  $\sim c_r^1$  for small values of  $c_r$ . In contrast, the curves level off for large values of  $c_r$ . There, regularizations become so rare that their effect can be neglected and the usual SPH noise is reached. In the middle panel, the noise error is plotted against  $h/\Delta$ . Here one finds that for the SPH limit, i.e. for  $c_r = 32$ , the noise error is well approximated by a relation  $\propto (h/\Delta)^{-2}$ . This means that the noise is directly related to the number of interacting neighbors. For smaller  $c_r$ , i.e. for an increasing number of regularizations, the noise seems to decrease even faster, according to  $\propto (h/\Delta)^{-2.5}$ . This may however be a selection effect if by chance the period of regularizations roughly coincide with the period of the data output. If so, the measured noise level is expected to be slightly smaller than the real noise level in the simulations. For the run with the higher number of regularizations, i.e.  $c_r = 1$ , the relation is again proportional to  $(h/\Delta)^{-2}$ . The lower panel of Figure 11 shows the dependence of the noise error on the smoothing length  $h$ . Here, the noise level is increasing nearly linearly with  $h$ . For the two-dimensional ring problem at hand, this means that accuracy increases roughly with the square root of the total particle number, making the maximum smoothing length an important parameter for accuracy.

## 5. Planet-disk interaction

In modern-day astronomy, numerical simulations play a vital role in understanding the underlying physical processes. It is therefore imperative that the methods are as reliable as possible. Validating and comparing different numerical methods on non-trivial problems is an important step in this process. Fortunately, several comparative studies relevant to astrophysical applications have been published (e.g. Kang et al. 1994; Bryden et al. 1999; Agertz et al. 2007). In VB06 17 different codes, among them 2 SPH codes, were compared on a problem involving planet-disk interaction. In this paper, we will adopt the set-up applied in VB06 for the inviscid case of both a Jupiter- and a Neptune-sized planet interacting with a Sun-like star. The mass of the star,  $M_*$  is set to unity while the mass of the planet,  $M_p$ , given by the ratio  $M_p/(M_* + M_p)$  is equal to  $10^{-3}$  and  $10^{-4}$  in the case of Jupiter and Neptune, respectively. The star and planet orbit the common center of mass (CM). The accretion disk itself is not self-gravitating, but interacts gravitationally with the central star and the planet. The planet’s gravitational potential has been softened using a softening parameter equal to  $0.03a$  (see VB06 for details), where  $a = 1$  is the orbital radius of the planet. The initial surface density of the disk is assumed to be

$$\Sigma_0 = 0.0002 \frac{M_*}{\pi a^2} \approx 6.366 \cdot 10^{-4}, \quad (19)$$

with inner and outer radii 0.4 and 2.5, respectively. The ratio of the local sound speed and Keplerian velocity is set to 0.05. The planet mass is gradually increased over the first 5 orbital periods as given by

$$M_p(t) = M_p \sin^2 \left( \frac{\pi t}{10P_p} \right) \quad (20)$$

to prevent strong shocks to dominate the early phases of the simulation. In all, the simulations were run for 100 planet orbital periods.

### 5.1. Numerical setup

This particular problem clearly lend itself to a cylindrical description. For this reason, nearly all the grid codes described in VB06, e.g. RH2D (Kley 1989), use cylindrical grids. Only 2 of the grid codes included in the comparison, FLASH-AP (Fryxell et al. 2000) and PENCIL (Brandenburg & Dobler 2002), used Cartesian grids. The two SPH codes included in VB06 are SPHTREE (Benz & Buchler 1990) and PARASPH (Schäfer et al. 2004). In the current work we have run simulations at 3 different resolution levels. Unlike the PENCIL, SPHTREE, and PARASPH simulations, the RSPH simulations do not explicitly apply any

artificial viscosity. The only viscous effect therefore comes from the regularization. Information regarding the resolution and execution time on a single processor for the 8 simulations just listed, can be found in Table 1. Unfortunately, the execution time for the FLASH-AP run is not available. It should also be noted that the high execution time of the PARASPH in part can be ascribed to the fact that this is a parallel code not optimized for single processor simulations. For the simulations included in VB06, but not listed in Table 1, the execution times range from roughly 1 to 42 hours.

The boundary conditions in the RSPH simulations are treated as in the PARASPH simulations. This means that the motion of particles found in the radial intervals of  $[0.4, 0.5]$  and  $[2.4, 2.5]$  is fixed to Keplerian orbits. In §4 it was shown how variation in the regularization period  $T_{\text{reg}}$  and  $h/\Delta$ , the number of particles per smoothing length, can affect the numerical dissipation. In this test,  $h/\Delta = 1.4$ , while the number of time steps between consecutive regularizations was allowed to vary according to a new optimization scheme described in Appendix A.

## 5.2. Interaction of Jupiter with a locally isothermal disk

It is well known that a planet orbiting a star at a fixed radius will open a considerable gap in the disk (Lin & Papaloizou 1986) and create a one-armed spiral wake (Ogilvie & Lubow 2002). The main features of this disk structure are established within a typical time interval of 10 orbital periods. However, to compare with the results presented in VB06, we ran the RSPH simulations for 100 orbital periods. In Figure 12 the surface density in logarithmic scale has been plotted as a function of the cylindrical coordinates (corresponding to Figure 2 and 10 in VB06). Panels marked *a*, *b*, and *c* correspond to the low, medium, and high resolution simulations, respectively. The dashed lines indicate the theoretical solution presented by Ogilvie & Lubow (2002). Already the low resolution results capture the main features of the interaction and fit reasonably well with the theoretical model. However, we see that characteristic features are sharpened and amplitudes are increased as resolution is increased. The cylindrical schemes presented in VB06 all produce solutions of the inviscid Jupiter system with local density enhancements in the gap associated with the  $L_4$  and  $L_5$  Lagrangian points. This is not seen in the corresponding solutions shown in Figure 12. Instead, the medium and high resolution RSPH simulations show clear indications of small scale wave structures in the gap in much the same way as that found in the inviscid FLASH-AP solution. In contrast, the PARASPH solution for the inviscid Jupiter system shows much less distinct features. The PENCIL and TREESPH scheme were not applied to the inviscid Jupiter system.

In order to get a more detailed picture of how the RSPH results fit in with both the viscous and inviscid results presented in VB06, we have in Figures 13 and 14 plotted cuts through the normalized surface density solutions for  $\phi = \pi$  and for  $r = a$ , respectively. In Figure 15 the azimuthally averaged surface density is plotted as a function of radius. Comparing with the appropriate figures in VB06, Figures 4-6 and 12-14, we see that the high resolution RSPH solution fits quite well with the overall picture seen in VB06. The peaks associated with the spiral arm wake are in Figure 13 sharp and their positions and amplitudes agree with that seen in VB06. The peaks found directly on either side of the gap are lower than what was reported in VB06 to be typical for the grid-based schemes. Also, the Lagrangian points are not seen in Figure 14. The mean density at  $r = a$  for  $\phi \neq 0$  is similar to that seen in VB06 for the viscous case. The azimuthally averaged density shown in Figures 15 and 16 reveals a drop in the density near the inner boundary layer at  $r = 0.5$ . As a result of this, the density peak found near the inner edge of the gap is lower than that found in almost all the grid-based solutions in VB06. On the other hand, the depletion in the high resolution case is not as distinct as that found for the two SPH schemes in VB06. The density peak found near the outer edge of the gap in the high and medium resolution RSPH runs fits well with that found by averaging over the grid-based results in VB06 for the inviscid case.

The solutions obtained with RH2D (Kley 1989) fit well with the mean solutions found in VB06 for both the viscous and inviscid case. To better illustrate the differences between the RSPH solutions and typical solutions presented in VB06, a direct comparison is presented in Figure 16 between the high resolution RSPH solution (solid line) and the viscous (dotted line) and inviscid (dashed line) RH2D solutions at 100 periods. The plotted quantity is the azimuthally averaged surface density as a function of radial position. This comparison confirms the depletion on the inside of the gap, a somewhat larger gap density caused mainly by the strong density peak near the planet, and a density peak on the outside of the gap which is somewhere in between the corresponding peaks in the viscous and inviscid RH2D solutions.

### 5.3. Interaction of Jupiter with a polytropic disk

How the disk dynamics can change with changing thermodynamical models, in particular in relation to self-gravitational stability, has been the focus of several studies in the last decade (Kley 1999; Pickett et al. 2000; Boss 2002; Klahr & Kley 2006). To show how RSPH deals with changing models, we present results from the simulation of a Jupiter-sized planet interacting with a  $\gamma = 1.4$  polytropic disk. We assume the same initial density and sound

speed profile as in the previous case. The ratio of the local sound speed to the Keplerian velocity is still chosen to be equal to 0.05. This implies the following, radially dependent equation of state

$$P = K(r)\rho^\gamma, \quad (21)$$

where  $K(r) = c_{s,0}^2(r)/(\gamma\Sigma_0^{\gamma-1})$ . This equation of state means that the initial pressure in the disk is reduced by the factor  $1/\gamma$ . In contrast, Kley (1999) assumed  $K$  to be a constant and let instead the ratio of local sound speed to Keplerian velocity to vary with radius.

This model has been run with the same particle number as the high resolution run described in the locally isothermal case. Figure 17 shows the resulting surface density profile after 100 orbital periods. The left hand panel shows the normalized surface density on a logarithmic scale and can be compared directly to the plots in Figure 12. Although the outer wave pattern is very similar, the gap density is seen to be considerably smaller. The right hand panel shows a direct comparison of the normalized density in the locally isothermal (dashed line) and the polytropic (solid line) cases. The plot shows the density as a function of normalized radius opposite the planet position. Apart from confirming the lower gap density in the polytropic case, the plot also indicates that the outer density peaks have been shifted slightly towards higher radii as a result of the change in thermodynamical model. The reduced gap density is consistent with a lower initial thermal pressure in the disk.

#### 5.4. Interaction of Neptune with a locally isothermal disk

The third planet-disk model simulated in this work deals with the interaction of the smaller, Neptune-sized planet with the locally isothermal disk described in the beginning of this section. Due to the factor 10 smaller planet mass, much smaller fluctuations in the disk density are expected. For the same reason, the spiral arms created by the planet should be in even better agreement with the theoretical model (Ogilvie & Lubow 2002). Once again, direct comparisons with VB06 is possible. The left hand plot of Figure 18 visualize the two-dimensional surface density for this case. The first thing to observe is the lack of a clearly defined gap. In contrast, the spiral arms are clearly visible and does follow nicely the theoretical predictions. Not surprisingly, noise associated with the inner boundary is more clearly visible in this case than what was the case in the two Jupiter simulations. The right hand panel of Figure 18 showing the density as a function of normalized radius opposite the planet position, confirms the impression formed by the left hand plot. This plot also confirms that the RSPH results fit much better with the typical grid results presented in VB06 rather than the PARASPH results presented in the same study.

## 6. Conclusion

We have in this paper studied the numerical dissipation in Regularized Particle Hydrodynamics (RSPH) simulations. The origin of the dissipation is the particle regularization scheme which allows the underlying particle distribution to be optimized at temporal intervals. In §3 we demonstrated the typical performance of RSPH on 3 basic hydrodynamical problems. The linear wave test in §3.1 showed how waves can become damped as a result of regularization unless the ratio of regularization period to wave period is considerably larger than unity. On the other hand, we also showed that the magnitude of the damping is usually small compared to the damping observed in standard SPH simulations which include artificial viscosity. The shock wave test in §3.2 confirms the impression from previous work that RSPH represents an improvement over SPH when it comes to describing shock waves. The last of the 3 basic hydrodynamical tests, the Kelvin-Helmholtz instability test, illustrates how numerical dissipation added during regularization can act constructively in improving the numerical description of multiphase flows. By smoothing the material interface, the perturbations are seen to grow, even without adding extra artificial conductivity (Price 2008).

In §4, comparisons with an analytical model of a viscously spreading ring allowed us to estimate the quantitative dependence of the mean effective viscosity on key numerical parameters. It was shown that the time between regularizations is indeed a key parameter in controlling both the numerical dissipation and the overall noise level. The general picture of the numerical viscosity obtained from the somewhat restricted test of the viscously spreading ring is qualitatively confirmed by the results from simulations of the more complex problem of the planet-disk interaction presented in §5. In this case  $h/\Delta$  is fixed to 1.4. The regularization period is allowed to vary automatically according to a new optimization scheme (see Appendix A). In §5.2, we studied a Jupiter-sized planet interacting with a locally isothermal disk. Simulations were performed at different resolution levels, where  $h$  was allowed to vary by a factor of 2 between the low and high resolution runs. The results from the 3 simulations were compared with that of other methods (presented in VB06). From this it was concluded that increasing the resolution not only had the effect of increasing amplitudes and sharpening interfaces and shock fronts. It was also pointed out that the wave structures seen within the gap in the medium and high resolution results resemble features seen in the inviscid planet-disk results presented in VB06. In contrast, the low resolution simulation produced a more uniform gap density, similar to the viscous planet-disk results in VB06. In §5.3 we explored the behaviour of the code when changing the thermodynamical model. The reduced pressure level in the polytropic disk caused the surface density in the gap to be reduced. We also saw in §5.4 that the RSPH method is able to handle reasonably well the more delicate problem of a Neptune-sized planet interacting with a locally isothermal disk.

The spiral waves are very well described, while the gap has more or less disappeared.

We have shown that regularization might be an attractive way to increase the accuracy in SPH simulations of protoplanetary disks. However, we have also clearly documented that this also adds numerical dissipation. The important question is therefore how do key parameters such as regularization period, ratio of smoothing length to particle spacing, and the smoothing length value itself affect the actual dissipation level. There are similar problems with e.g. artificial viscosity and/or conductivity. How can we relate the physical dissipation level to the numerical parameters? The same level of viscosity cannot be used in the linear wave test as in the strong shock test. A common approach in this regard is to use switching mechanisms that turn for instance artificial viscosity down when it is not needed. In choosing an optimal regularization period, one must consider both how the numerical dissipation might affect the total dissipation and therefore alter the physical model, but also what upper limit of the noise level is needed in order to achieve acceptable resolution. As long as only the regularization period is allowed to vary, these two requirements will be in competition. However, by increasing the number of particles per characteristic length scale for the problem at hand, both low numerical dissipation and low noise level can be achieved at the same time.

In situations where shocks or other types of discontinuities are present in the flow field, the characteristic length scale in the numerical representation will be proportional to the smoothing length,  $h$ . Increasing the number of particles per characteristic length scale can therefore only be achieved by increasing  $h/\Delta$ , the number of particles per smoothing length. If on the other hand the characteristic length scale of the physical problem is truly resolved by the numerical representation, a decrease in both the numerical dissipation and numerical noise can be achieved either by decreasing  $h$  or by increasing  $h/\Delta$ . The main conclusion from this work is therefore: The regularization period should be considerably higher than the wave period of any important wave modes. In problems where a range of important modes exist, the mode with the longer period should determine the regularization period. If it is important to reduce the dissipation to a minimum, a relatively large  $h/\Delta$  should be chosen. Bear in mind though that for linear problems,  $h/\Delta$  must be close to 1.2 to secure stability. Alternatively,  $h$  itself can be reduced in problems which do not involve discontinuities. In multiphase flow problems, dissipation due regularization can improve the description. Choosing a relatively small  $h/\Delta$ , e.g.  $h/\Delta = 1.2$ , is therefore recommendable.

The overall goal of any numerical scheme is to produce numerical solutions with acceptable accuracy at the lowest possible cost. In this context this often means reducing both the numerical dissipation and the numerical noise with as large  $h$  and as small  $h/\Delta$  as possible. The question is therefore whether modifications to the RSPH scheme can be made to

improve the performance of the method with regards to accuracy in relatively low Reynolds number flow. As a continuation of this work, we would in future like to consider two possible approaches. The first approach addresses the viscous transformation of kinetic energy into thermal energy which in the current version of the method occurs during regularization. Conservation of linear momentum prevents kinetic energy to be conserved when transferring momentum from the old to the new particles. Instead of compensating the loss in kinetic energy by an equal increase in thermal energy, one could in principle set up an artificial interaction between the new particles which would preserve the momentum but would correct the kinetic energy. The other approach we plan to investigate, is to generalize the scheme for producing the new particle positions. So far, we have assumed that  $h/\Delta$  is a global constant. If  $h/\Delta$  must be increased due to requirements of low numerical dissipation and noise, this might be computational expensive. If, on the other hand,  $h/\Delta$  could be increased locally in regions where numerical dissipation is required to be small, the reduction in numerical dissipation could be achieved at a lower computational cost. The main cost would be added code complexity.

The authors would like to thank Prof. Wilhelm Kley for providing the RH2D data and to Mr. Audun Bjerke for running the AUTODYN software on the strong shock test. This work received support in part from the Research Council of Norway and the Deutsche Forschungsgemeinschaft DFG through grant DFG Forschergruppe 759 “The Formation of Planets: The Critical First Growth Phase”.

### A. Variable regularization intervals

In the shock simulations described in §3.2 and the planet-disk simulations described in §5 we experimented with a scheme that would allow the time intervals between regularizations to adapt automatically to the dynamics of the problem. The idea has been to design a scheme which monitors the local particle number density,  $n$ , and activates regularization whenever the estimate of  $n$  becomes too small or too large, or when the spread of  $n$  within an interaction sphere becomes too large. Here we will quickly describe this scheme: First we calculate the particle number density

$$n_a = \sum_{b \neq a} \mathcal{W}_{ab}. \quad (\text{A1})$$

Note that we have omitted the contribution from the particle itself,  $\mathcal{W}_{aa}$ . This has been done to get a more precise picture of how the local number density varies, especially when

the number density drops. From  $n_a$  we estimate the number of interacting neighbors as

$$N_a = V(h_a)n_a, \quad (\text{A2})$$

where  $V(h_a)$  is the interaction volume (area in two dimensions). We also estimate the local variation in neighbor number,  $\delta N$ , from the expression

$$\delta N_a^2 = \left( \frac{N_a - \langle N \rangle_a}{N_a} \right)^2, \quad (\text{A3})$$

where

$$\langle N \rangle_a = \sum_b \frac{m_b}{\rho_b} N_b \mathcal{W}_{ab}. \quad (\text{A4})$$

Regularization is invoked if, for any particle  $a$ , at least one of the following conditions hold:

$$N_a < N_{\min}, N_a > N_{\max}, \quad (\text{A5})$$

or

$$\delta N_a > \delta N_{\max}. \quad (\text{A6})$$

In the shock test described in §3.2,  $N_{\min} = 9.5$  (corresponds roughly to  $h/\Delta = 1.1$ ),  $N_{\max} = 308$  (corresponds roughly to  $h/\Delta = 5.0$ ), and  $\delta N_{\max} = 0.4$ . In addition, the maximum number of time steps allowed between consecutive regularizations is set to 128. In the planet-disk test described in §5, the parameters chosen are  $N_{\min} = 4.5$  (corresponds roughly to  $h/\Delta = 0.9$ ),  $N_{\max} = 107$  (corresponds roughly to  $h/\Delta = 3.0$ ), and  $\delta N_{\max} = 0.8$ . Maximum number of time steps between consecutive regularizations is set to 160. In both cases, typical regularization periods are between 50 and 100. The conclusion so far is that the scheme, as it is formulated here, requires considerable fine-tuning for it to provide a really useful alternative to just using a fixed interval between regularizations.

## REFERENCES

- Aarseth, S. J. 1963, *ApJ*, 228, 664
- Agertz, O. et al. 2007, *MNRAS*, 380, 963
- Benz, W. & Buchler, J. R. 1990, in *Numerical Modelling of Nonlinear Stellar Pulsations: Problems and Prospects* (Dordrecht: Kluwer)
- Børve, S., Omang, M., & Trulsen, J. 2001, *ApJ*, 561, 82
- Børve, S., Omang, M., & Trulsen, J. 2004, *ApJS*, 153, 447 (Paper I)

- Børve, S., Omang, M., & Trulsen, J. 2005, *J. Comput. Phys.*, 208, 345 (Paper II)
- Børve, S., Omang, M., & Trulsen, J. 2006, *ApJ*, 652, 1306 (Paper III)
- Børve, S., Bjerke, A., Omang, M., & Trulsen, J. 2008, in *ERCOFTAC SIG SPHERIC IIIrd Int. Workshop*, ed. P. Maruzewski, 192
- Børve, S. & Price, D. 2009, in *ERCOFTAC SIG SPHERIC IVth Int. Workshop*, in press
- Boss, A. P., *ApJ*, 576, 462
- Brandenburg, A. & Dobler, W. 2002, *Comp. Phys. Comm.*, 147, 471
- Bryden, G., Chen, X., Lin, D. N. C., Nelson, R. P., & Papaloizou, J. C. B. 1999, *ApJ*, 514, 344
- de Val-Borro, M. et al. 2006, *MNRAS*, 370, 529 (VB06)
- Flebbe, O., Münzel, S., Herold, H., Riffert, H. & Ruder, H. 1994, *ApJ*, 431, 754
- Fryxell, B. A. et al. 2000, *ApJS*, 131, 273
- Gingold, R. A., & Monaghan, J. J. 1977, *MNRAS*, 181, 375
- Imaeda, Y. & Inutsuka, S.-I. 2002, *ApJ*, 569, 501
- Kang, H., Ostriker, J. P., Cen, R., Ryu, D., Hernquist, L., Evrard, A. E., Bryan, G. L., & Norman, M. L. 1994, *ApJ*, 430, 83
- Klahr, X. & Kley, W. 2006, *A&A*, 445, 747
- Klein, R. I. 1999, *J. Comput. Appl. Math.* 109, 123
- Kley, W. 1989, *A&A*, 208, 98
- Kley, W. 1999, *MNRAS*, 303, 696
- Lin, D. N. C. & Papaloizou, J. 1986, *ApJ*, 307, 395
- Lucy, L. B. 1977, *AJ*, 82, 1013
- Lüst, R. 1952, *Zeitschrift für Naturforschung*, 7a, 87
- Lynden-Bell, D. & Pringle, J.E. 1974, *MNRAS*, 168, 603
- Mayer, L., Quinn, T., Wadsley, J., & Stadel, J. 2002, *Science*, 298, 1756

- Meglicki, Z., Wickramasinghe, D. & Bicknell, G. V. 1993, MNRAS, 264, 691
- Monaghan, J. J. 2006, MNRAS, 365, 199
- Monaghan, J. J. 2005, Rep. Prog. Phys., 68, 1703
- Monaghan, J. J. 1989, J. Chem. Phys., 82, 1
- Monaghan, J. J. & Gingold, R. A. 1983, J. Chem. Phys., 52, 374
- Mori, M. & Burkert, A. 2000, ApJ, 538, 559
- Morris, J. P. 1996a, Publ. Astron. Soc. Aust., 13, 97
- Morris, J. P. 1996b, Analysis of Smoothed Particle Hydrodynamics with Applications (PhD thesis) (Melbourne: Monash University)
- Murray, S. D., White, S. D., Blondin, J. M., & Lin, D. N. C. 1993, ApJ407, 588
- Ogilvie, G. I. & Lubow, S. H. 2002, MNRAS, 330, 950
- Omang, M., Børve, S., & Trulsen, J. 2006, J. Comput. Phys., 213, 391
- Omang, M., Christensen, S. O., Børve, S., & Trulsen, J. 2009, Shock Waves, DOI: 10.1007/S00193-009-0196-8
- O'Rourke, J. 1998 Computational Geometry in C (2d ed.; Cambridge: Cambridge University Press)
- Pickett, B. K., Cassen, P., Durisen, R. H., & Link, R, 2000, ApJ, 529, 1034
- Price, D. & Bate, M.R. 2007, MNRAS, 377, 77
- Price, D. & Monaghan, J.J. 2007, MNRAS, 374, 1347
- Price, D. 2008, J. Comput. Phys., 227, 10040
- Pringle, J. E. 1981, ARA&A, 19, 137
- Schäfer, C., Speith, R., Hipp, M., & Kley, W. 2004, A&A, 418, 325
- Speith, R. & Kley, W. 2003, A&A, 399, 395
- Speith, R. & Riffert, H. 1999, J. Comput. Appl. Math., 106, 231

Whitehouse, S.C., Bate, M.R., & Monaghan, J.J. 2005, MNRAS, 364, 1367

Xiao, F. 2004, J. Comput. Phys., 195, 629

Table 1. Comparison of simulation size and computational efficiency

Name	Size	Processor	Time (hr)
RH2D	$128 \times 384$	P4 3 GHz	3.4
FLASH-AP	$320 \times 320$	Athlon 1.8 GHz	-
PENCIL	$640 \times 640$	P4 2.4 GHz	36
SPHTREE	250.000	Opteron 1.8 GHz	10
PARASPH	350.000	Opteron 2.0 GHz	250
RSPH (LOW)	48.000	Intel Xeon 3.2 GHz	4.8
RSPH (MED)	108.000	Intel Xeon 3.2 GHz	14.3
RSPH (HIGH)	191.000	Intel Xeon 3.2 GHz	33.5

Note. — Information about the computational size (grid size or particle number), the processor type used, and approximate execution time for 5 selected simulations described in VB06 and 3 RSPH simulations described in the current work.

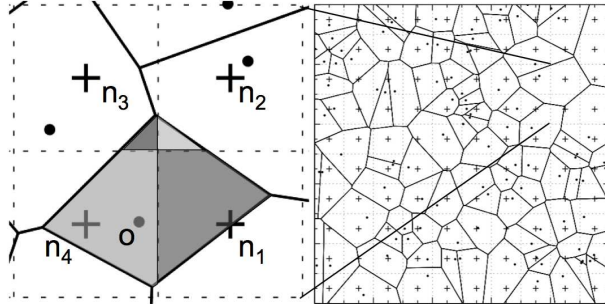


Fig. 1.— Toy-example illustrating the process of mapping properties from one particle distribution to the next. Here, the location of the old and new particles are indicated by the dots and the plus signs, respectively. The left hand plot illustrates how the new particles  $n_1 - n_4$  all overlap with the old particle  $o$  and therefore divide the mass, momentum, and internal energy of the latter particle between themselves in the regularization process.

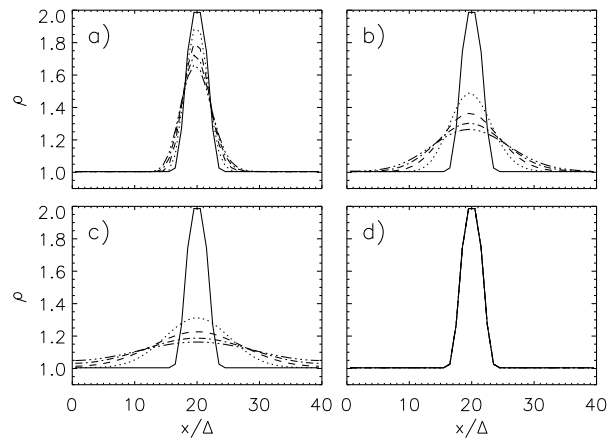


Fig. 2.— Numerical diffusion due to regularization in a force-free, one-dimensional problem where the ratio  $T_{reg}v_d/\Delta$  in simulations  $a$ ,  $b$ ,  $c$ , and  $d$  is equal to 0.01, 0.1, 0.5, and 1.0, respectively.

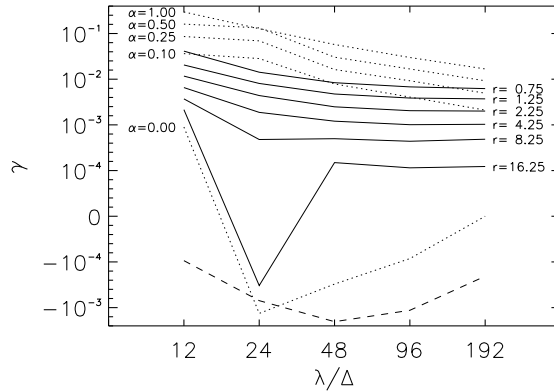


Fig. 3.— Estimated damping rate ( $\gamma$ ) in the linear wave test as a function of wave length. The solid lines represent runs where regularization has been performed ( $r$  is the ratio of regularization period to wave period), the dotted lines represent runs where artificial viscosity but no regularization is applied ( $\alpha$  is the primary viscosity parameter). Finally, the dashed line represents results using the RH2D grid code.

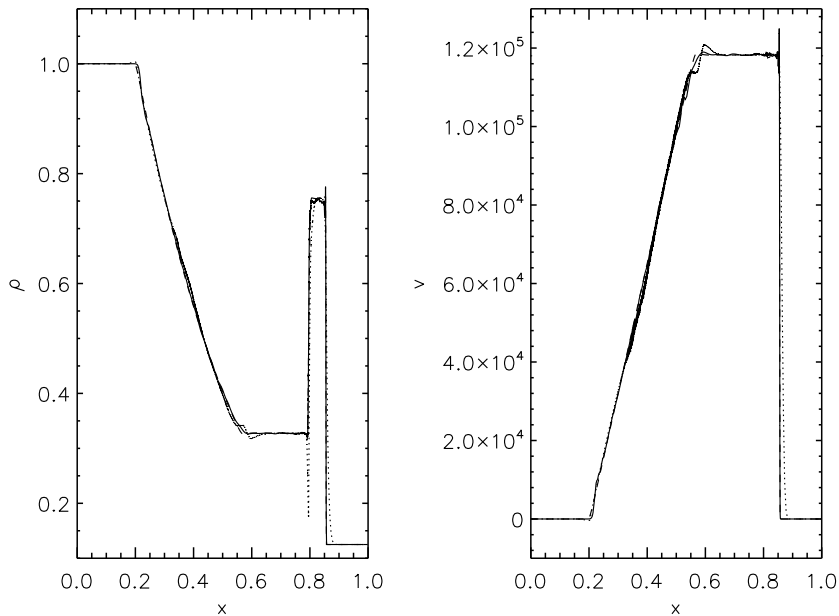


Fig. 4.— Density (left panel) and velocity (right panel) profiles for the extreme shock test at  $t = 2.5 \cdot 10^{-6}$ . The solid, dotted, and dashed lines represent RSPH, SPH, and AUTODYN FCT solutions, respectively.

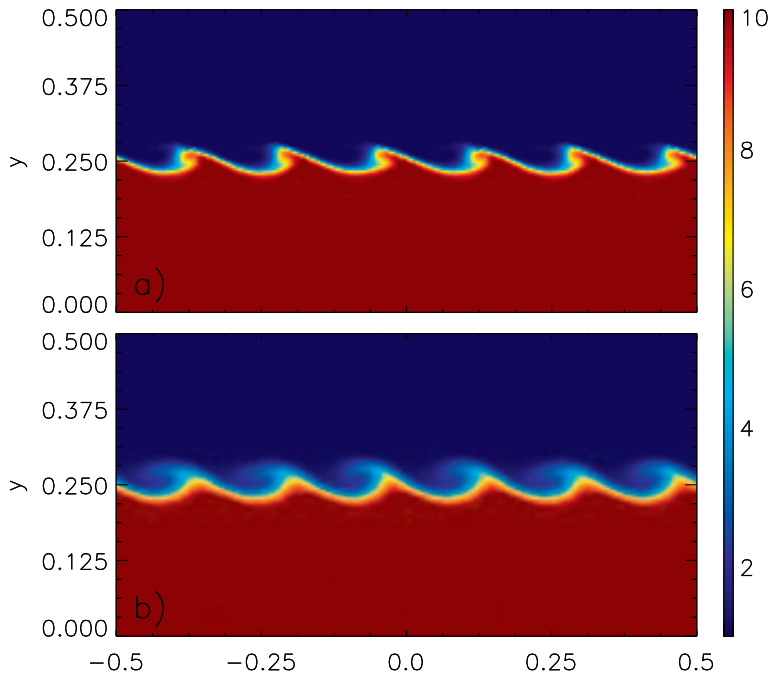


Fig. 5.— Density at time  $t = \tau_{\text{KH}}$  in the Kelvin-Helmholtz instability test using RSPH. The upper and lower plots represent the solutions obtained without and with artificial conductivity, respectively.

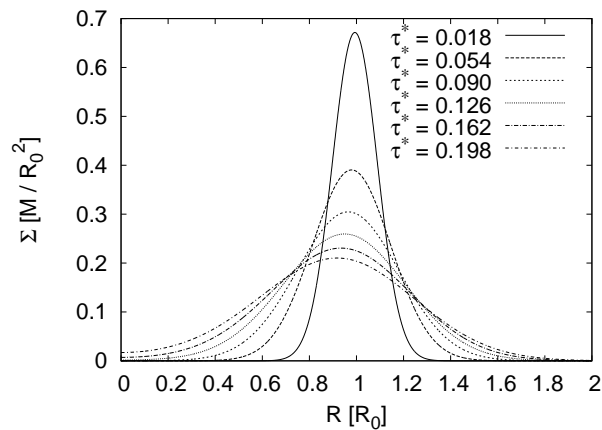


Fig. 6.— Time evolution of the surface density distribution of the viscous ring, measured in viscous time  $\tau^*$ .

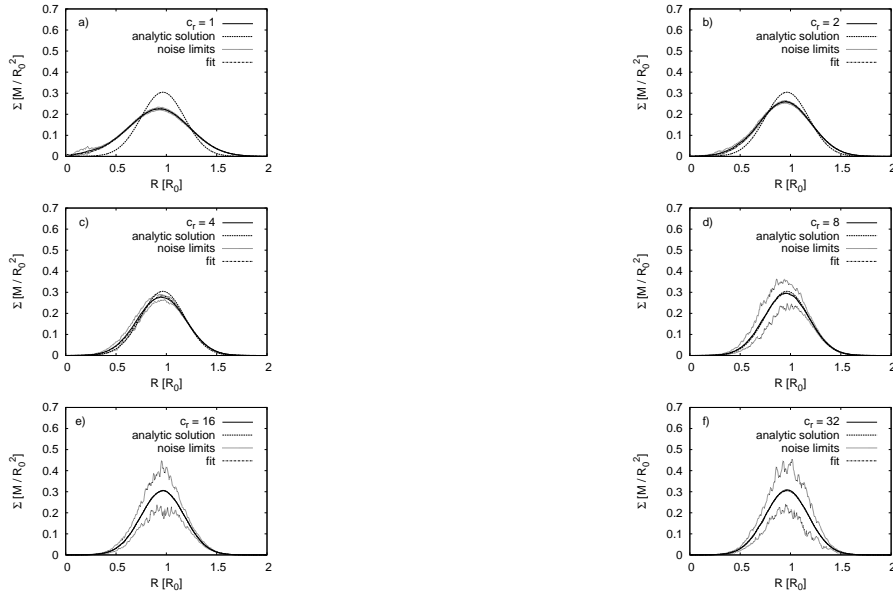


Fig. 7.— Dependence of the RSPH simulation results on the number of regularizations. Plotted is the azimuthally averaged surface density (solid line) with maximum and minimum noise level (dotted lines) compared with the analytic solution at viscous time  $\tau^* = 0.090$  (dashed line) and a fit of the analytic solution at the effective viscous time measured (dashed-dotted line). The parameter  $c_r$  is varied from 1 to 32 for fixed  $h/\Delta = 1.6$  and  $h = 0.02$  (in units of  $R_0$ ).

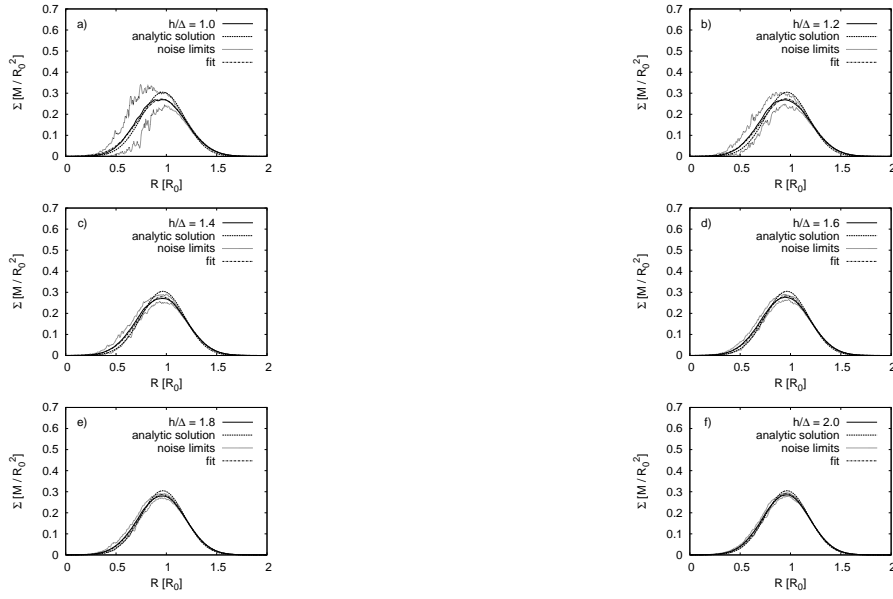


Fig. 8.— Dependence of the RSPH simulation results on the number of particles per smoothing length. Plotted is the azimuthally averaged surface density (solid line) with maximum and minimum noise level (dotted lines) compared with the analytic solution at viscous time  $\tau^* = 0.090$  (dashed line) and a fit of the analytic solution at the effective viscous time measured (dashed-dotted line). The parameter  $h/\Delta$  is varied from 1.0 to 2.0 for fixed  $c_t = 4$  and  $h = 0.02$  (in units of  $R_0$ ).

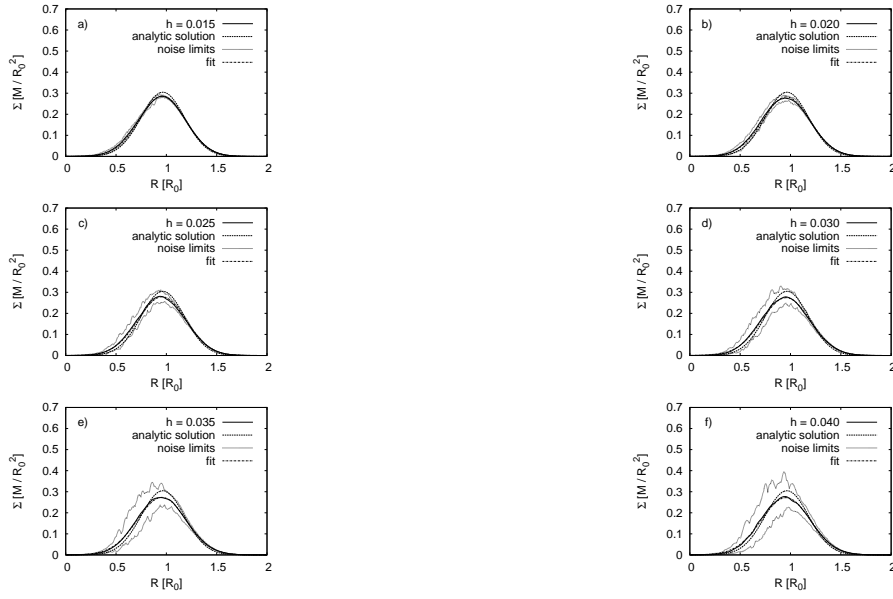


Fig. 9.— Dependence of the RSPH simulation results on the smoothing length. Plotted is the azimuthally averaged surface density (solid line) with maximum and minimum noise level (dotted lines) compared with the analytic solution at viscous time  $\tau^* = 0.090$  (dashed line) and a fit of the analytic solution at the effective viscous time measured (dashed-dotted line). The parameter  $h$  is varied from 0.015 to 0.04 (in units of  $R_0$ ) for fixed  $c_r = 4$  and  $h/\Delta = 1.6$ .

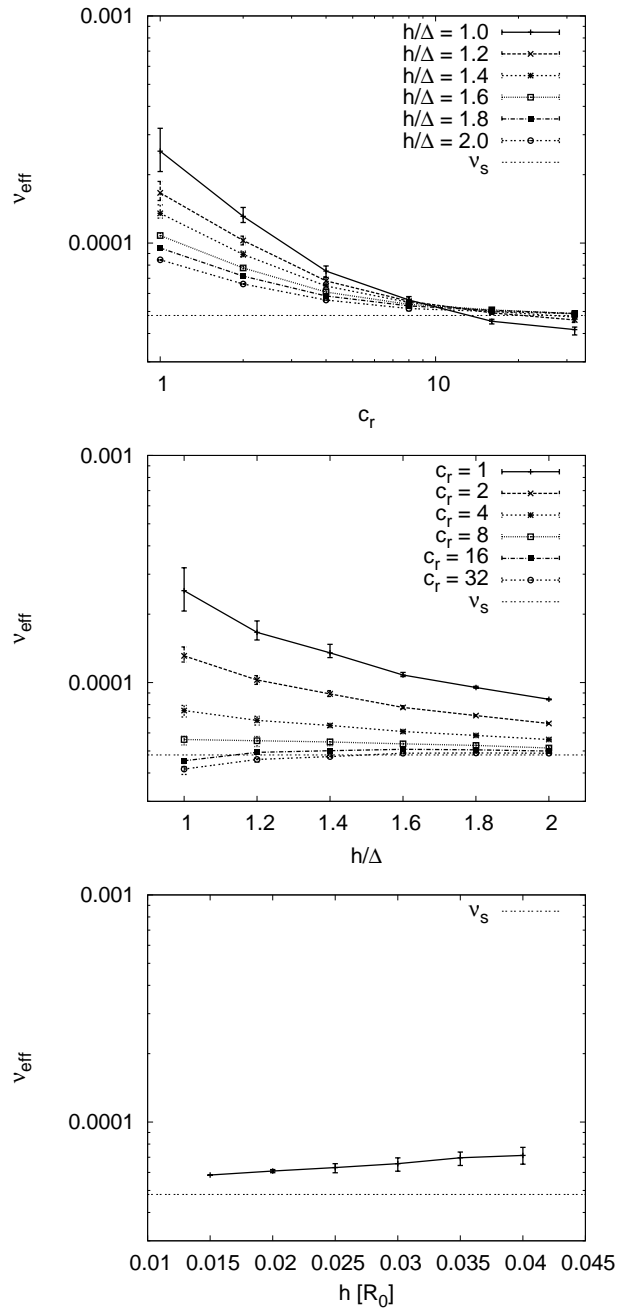


Fig. 10.— Measured effective viscosity  $\nu_{\text{eff}}$  depending on the length of the regularization cycle  $c_r$  (upper panel), on the number of particles per smoothing length  $h/\Delta$  (middle panel), and on the maximum smoothing length  $h$  (lower panel).

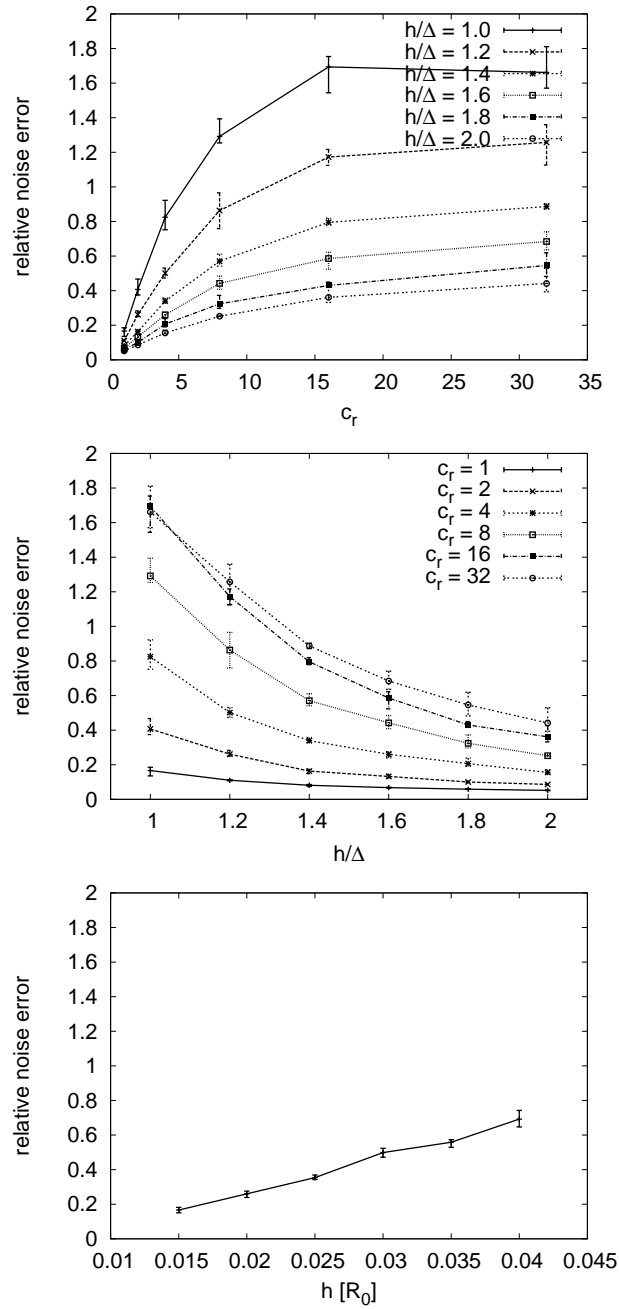


Fig. 11.— Relative error due to noise depending on the length of the regularization cycle  $c_r$  (upper panel), on the number of particles per smoothing length  $h/\Delta$  (middle panel), and on the maximum smoothing length  $h$  (lower panel).

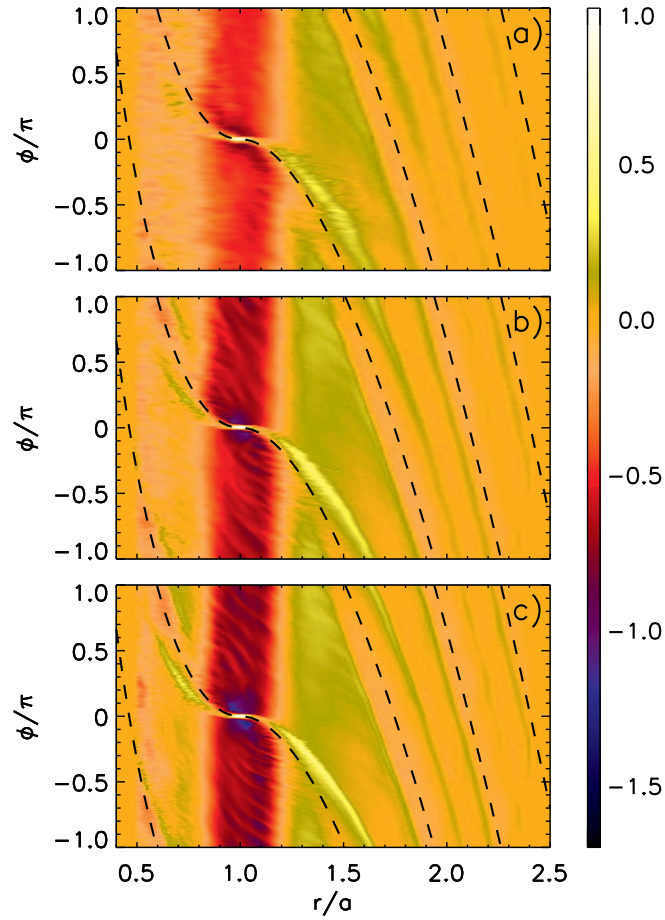


Fig. 12.— Surface density in logarithmic scale after 100 orbital periods for the low (*a*), medium (*b*), and high (*c*) resolution simulations of a Jupiter-sized planet interacting with a locally isothermal disk. The density scale ranges between  $-1.7 < \log(\Sigma/\Sigma_0) < 1.0$ .

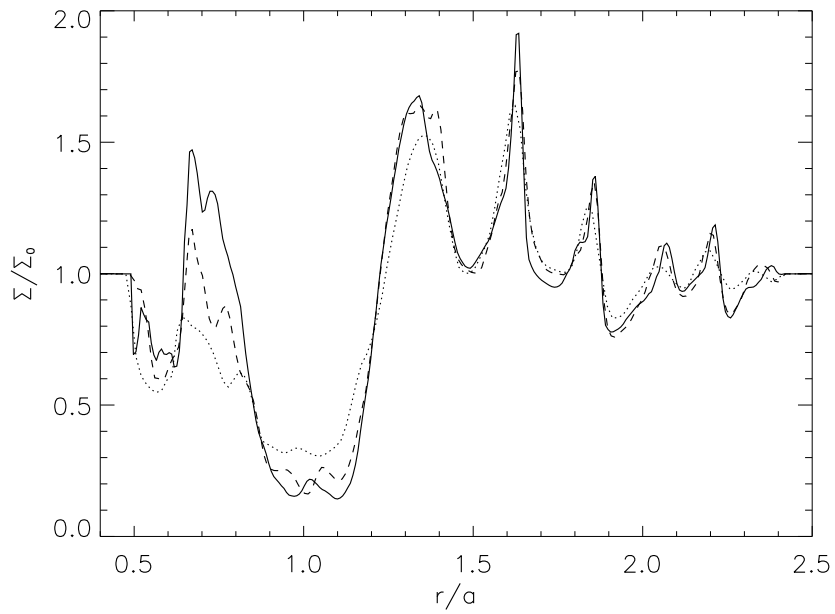


Fig. 13.— Surface density profiles as a function of normalized radius opposite to the planet position ( $\phi = \pi$ ) after 100 orbital periods in the case of the Jupiter-sized planet interacting with a locally isothermal disk. The solid, dashed, and dotted lines represent the high, medium, and low resolution results, respectively.

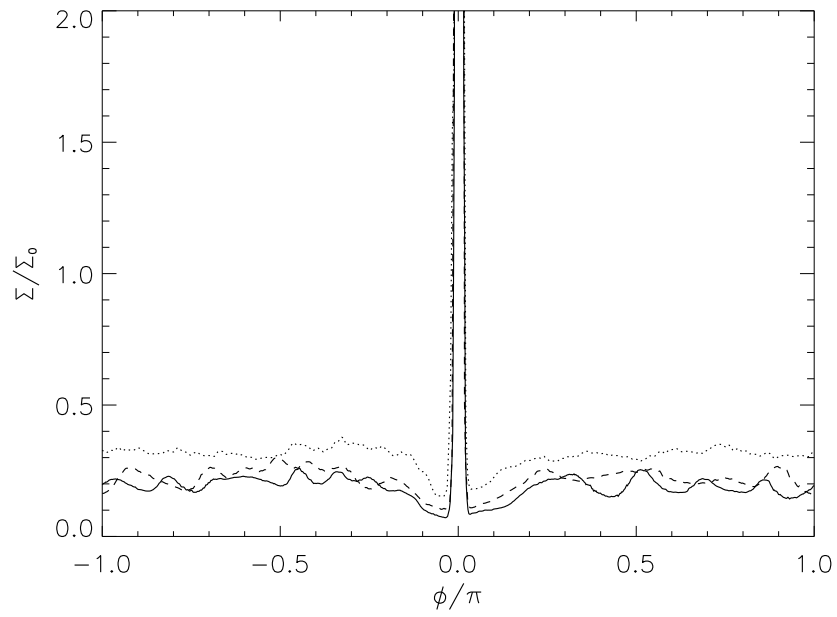


Fig. 14.— Surface density profiles as a function of the azimuthal position at the radius of the planet orbit after 100 orbital periods in the case of the Jupiter-sized planet interacting with a locally isothermal disk. The solid, dashed, and dotted lines represent the high, medium, and low resolution results, respectively.

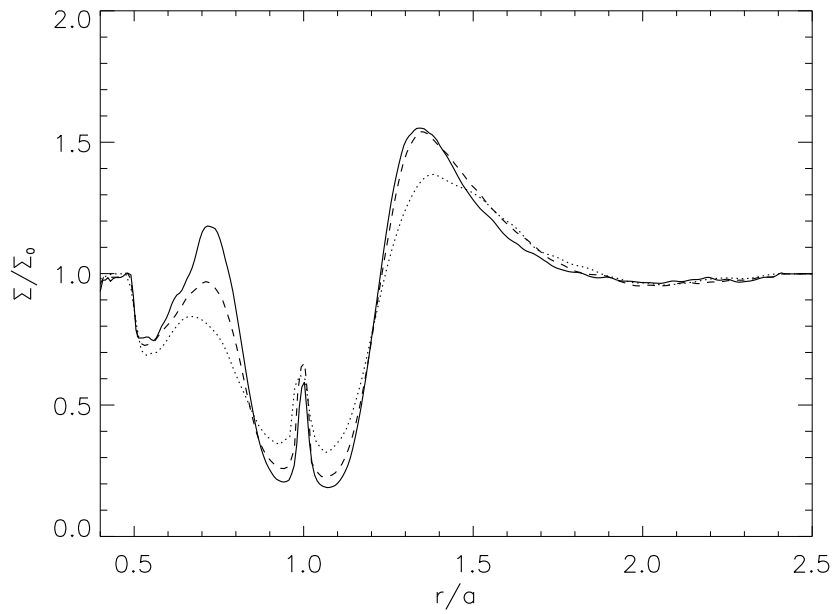


Fig. 15.— Azimuthally averaged, normalized surface density as a function of radial position after 100 orbital periods in the case of the Jupiter-sized planet interacting with a locally isothermal disk. The solid, dashed, and dotted lines represent the high, medium, and low resolution results, respectively.

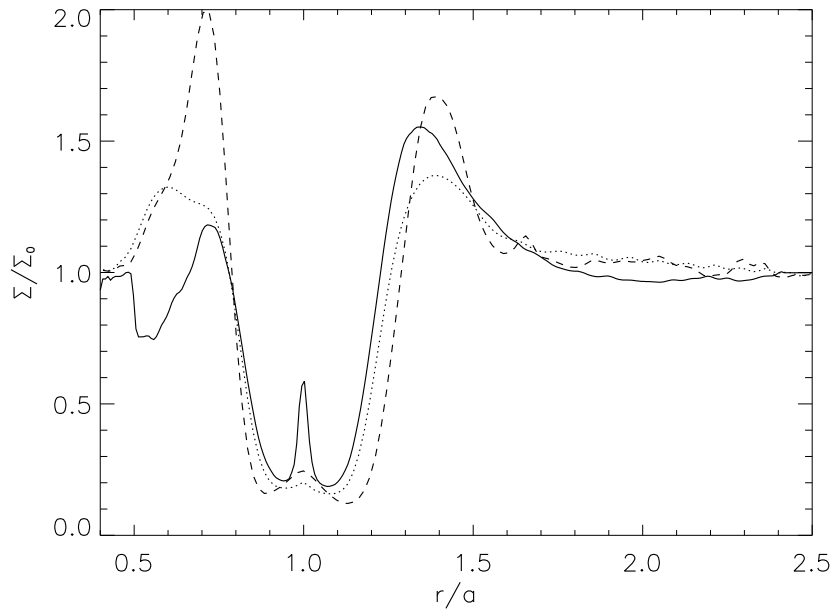


Fig. 16.— Comparison between the high resolution RSPH solution (solid line) and the viscous (dotted line) and inviscid (dashed line) solutions obtained with the cylindrical grid code RH2D (Kley 1989). The compared quantity is the azimuthally averaged, normalized surface density as a function of radial position after 100 orbital periods in the case of the Jupiter-sized planet interacting with a locally isothermal disk.

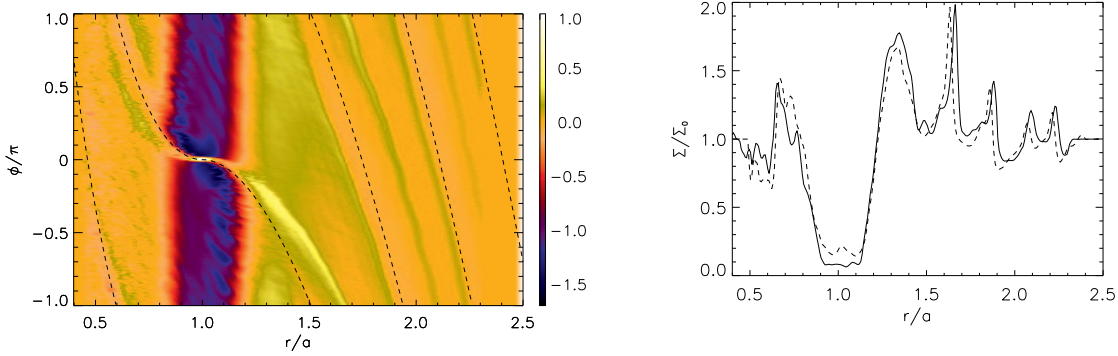


Fig. 17.— Left panel shows surface density in logarithmic scale ( $-1.7 < \log(\Sigma/\Sigma_0) < 1.0$ ) after 100 orbital periods for the case of a Jupiter-sized planet interacting with a polytropic disk. Right panel shows a comparison between the normalized surface density profiles from the high resolution locally isothermal (dashed line) and the polytropic (solid line) runs plotted as a function of normalized radius opposite to the planet position ( $\phi = \pi$ ) after 100 orbital periods .

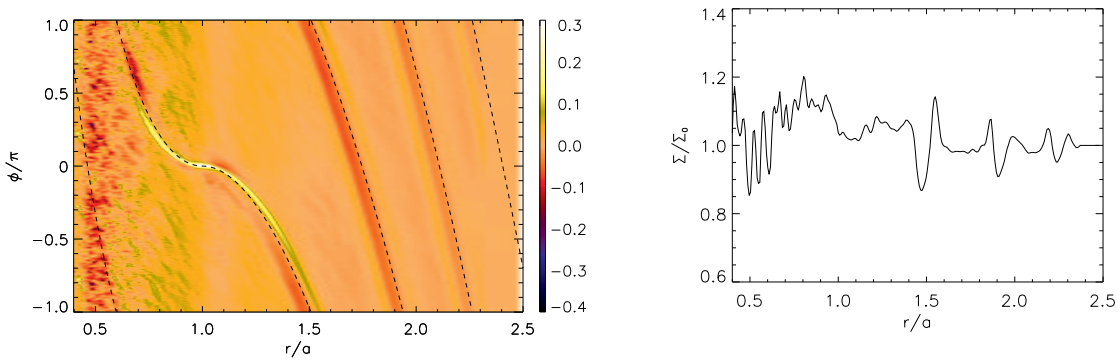


Fig. 18.— Left panel shows surface density in logarithmic scale ( $-0.4 < \log(\Sigma/\Sigma_0) < 0.3$ ) after 100 orbital periods for the case of a Neptune-sized planet interacting with a locally isothermal disk. Right panel shows normalized density profile as a function of normalized radius opposite to the planet position ( $\phi = \pi$ ) after 100 orbital periods .